Structure of cholesterol helical ribbons and self-assembling biological springs

Boris Khaykovich[†], Chintan Hossain[‡], Jennifer J. McManus[§], Aleksey Lomakin[§], David E. Moncton[†‡], and George B. Benedek[‡§¶‖]

[†]Nuclear Reactor Laboratory, Massachusetts Institute of Technology, 138 Albany Street, Cambridge, MA 02139; and [‡]Department of Physics, [§]Materials Processing Center, and [¶]Center for Materials Science and Engineering, Massachusetts Institute of Technology, 77 Massachusetts Avenue, Cambridge, MA 02139

Contributed by George B. Benedek, April 9, 2007 (sent for review February 9, 2007)

We report the results of x-ray-scattering studies of individual helical ribbons formed in multicomponent solutions of cholesterol solubilized by various surfactants. The solutions were chemically defined lipid concentrate (CDLC) and model bile. In these and many analogous multicomponent surfactant–cholesterol solutions, helical ribbons of two well defined pitch angles, namely 11° and 54°, are formed. We have suggested previously that this remarkable stability results from an underlying crystalline structure of the sterol ribbon strips. Using a synchrotron x-ray source, we have indeed observed Bragg reflections from individual ribbons having 11° pitch angle. We have been able to deduce the parameters of the unit cell. The crystal structure of these ribbons is similar to that of cholesterol monohydrate, with the important difference that the length of the unit cell perpendicular to the cholesterol layers is tripled. We discuss possible origins for this triplication as well as the connection between the crystalline structure and the geometrical form of the helical ribbons.

crystal structure | x-ray diffraction | crystallization | surfactants

Self assembly of helical ribbons in complex fluids is an interesting phenomenon, which poses fundamental questions about the molecular structure, elastic properties, and kinetic evolution of these objects. In particular, quaternary solutions, which contain cholesterol, nonionic surfactants, and lipids, spontaneously form helical ribbons with characteristic pitch angles of 11° and 54°. These helical ribbons are long rectangular strips, which curl along a cylindrical surface. These objects were discovered in human gallbladder bile, where they form spontaneously upon the dilution of bile. This dilution produces a solution supersaturated with respect to cholesterol (1). Formation of similar helical ribbons has been later reported in >20 different solutions with various sterols analogous to cholesterol, surfactants, and phospholipids or fatty acids (2). These helical ribbons form in a variety of axial lengths, widths, and radii. Remarkably, however, almost all have pitch angles of either 11° or 54°.

Several theoretical models have been proposed to explain the formation and properties of helical ribbons, which sometimes form in complex fluids containing chiral amphiphilic molecules (3–10). These theories were designed to describe the helical ribbons in solutions containing a single species of phospholipids, which can form bilayers. Therefore, the ribbons were modeled theoretically as fluid bilayers, where hydrophobic carbon chains are sandwiched between hydrophilic head groups. Calculations of the properties of such membranes are usually based on the curvature elasticity model (11), which is founded on general physical arguments about the dependence of the fluid membrane elastic free energy on its curvature. Based on this model, subsequent theories attempted to explain the geometrical and elastic properties of the helical ribbons. For example, the formation of helices is attributed to boundary effects [such as polarization-induced edge charges (12)], formation of topological defects in the in-plane orientational order (13) and the effects of molecular tilt on spontaneous curvature (14). Another class of theories explicitly includes the effects of molecular chirality or spontaneous chiral symmetry breaking within the membrane, based on analogies to chiral liquid crystals (15–21).

These theories are apparently not applicable to our multicomponent surfactants-lipids-sterol-water systems. Some of the most important observations are not readily explained by using the existing models. These observations are as follows. (*i*) Helical ribbons of the same pitch angles, 11° and 54°, have been observed in >20 solutions with variable sterols and surfactants. (*ii*) Sterols dominate the chemical composition of our strips (2). (*iii*) Our ribbons are much thicker than even multilamellar phospholipid membranes. From colored interference patterns, we expect that some of the helical ribbons reach the thickness of several microns. (*iv*) Sterols are hydrophobic and therefore must be covered by surfactants on the surface of the strips. At the same time, these surfactants do not play a key role in determining the ribbon geometry. Indeed, it was found that removal of phospholipid surfactants did not affect the ribbons' geometry in the model bile (22). All these observations and the fact that the helical ribbons are metastable intermediates on the pathway of cholesterol crystallization in supersaturated solutions (1, 18, 23, 24) point to the possibility that an organized, crystalline cholesterol structure within the strip, rather than the surfactant layers, determines the external form of our helical ribbons. Indeed, in ref. 25, the structure of the elastic free energy needed to explain our experimental findings was based on a crystal model for the strip. To directly test this crystal model, we undertook x-ray diffraction measurements designed to probe directly the structure of the individual strips, which form helical ribbons. Our experiments show that the strips are, in fact, single crystals. Their crystal structure is similar to that of cholesterol monohydrate (ChM) but with an unusual superlattice structure along one of the crystalline axes. Our results are consistent with the findings of recent electron diffraction studies of submicron-size ribbons in model bile (24).

The geometry of the helical ribbons is characterized by the radius (R), width (w), thickness (t), contour length (s), and pitch angle (ψ) (see figure 1*a* in ref. 18). The axial length of a ribbon is $l = s\,sin(\psi)$. In the crystalline model, the pitch angle is given by ref. 25

$$\psi = \arctan\left(\sqrt{K_\alpha / K_\gamma}\right). \qquad [1]$$

The coefficients K_α and K_γ are combinations of the coefficients of the elastic modulus tensor. K_α is associated with the bending of lines

Author contributions: B.K., D.E.M., and G.B.B. designed research; B.K., C.H., and J.J.M. performed research; B.K., C.H., A.L., and D.E.M. analyzed data; and B.K., A.L., D.E.M., and G.B.B. wrote the paper.

The authors declare no conflict of interest.

Abbreviations: CDLC, chemically defined lipid concentrate; ChM, cholesterol monohydrate.

‖To whom reprint requests should be addressed. E-mail: benedek@mit.edu.

www.pnas.org/cgi/doi/10.1073/pnas.0702967104

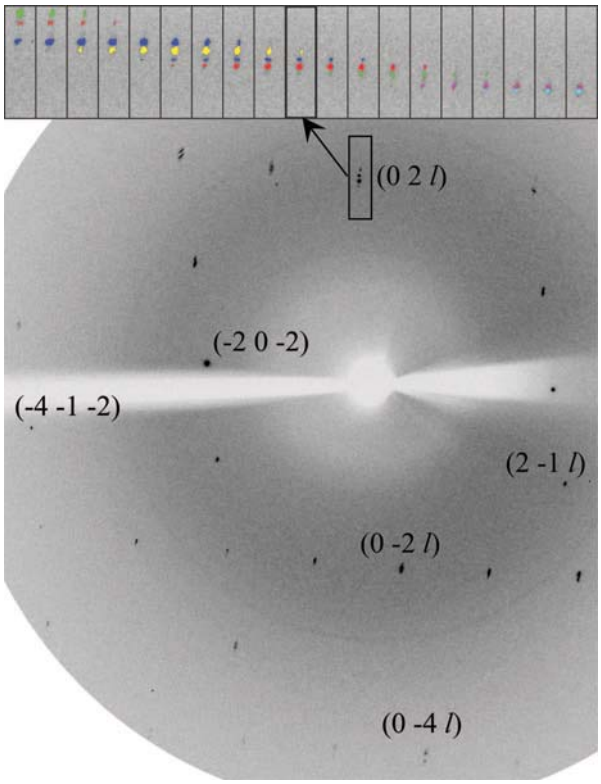

Fig. 1. A portion of the diffraction pattern produced by a strip formed in CDLC. The numerical readout from a 12-bit CCD camera was used in our data analysis. The image shown above is the experimental readout converted into an 8-bit gray-scale image, with brightness and contrast scales appropriately adjusted. The rectangle shows a particular area of the image that contains a group of closely spaced Bragg spots. *Inset* shows a collection of such rectangular areas taken from images for 19 sequential angular orientations of the sample. These orientations are 1° apart. All areas in *Inset* are from the same location in each image. Each Bragg peak, labeled by a unique color, spans about six areas, thereby forming ''Bragg arcs.'' Our software identifies each spot location using manual control if necessary. The center of the Bragg arc in reciprocal space coordinates is then found by an intensity-weighted averaging of the positions of pixels from each spot using the CCD data. The Bragg arcs shown in *Inset* by different colors correspond to Miller indices: (0 2 *l*), where *l* is between −17 and −7.

parallel to the contour length and K_γ with the bending of lines parallel to the width. On the other hand, the radius (R) is due to a balance between strip elasticity and a spontaneous bending force. This force arises from different interfacial energies of the two opposite faces of a strip constituted of asymmetrical cholesterol molecules.

Results

We have measured low-pitch ribbons both from chemically defined lipid concentrate (CDLC) and a model bile. For x-ray diffraction measurements, the ribbons from CDLC were stretched and mounted on a thin nylon loop in air, as explained in *Materials and Methods*. These ribbons demonstrated clear diffraction patterns. Fig. 1 shows a typical example of a diffraction pattern for a particular orientation of the sample. Fig. 1 *Inset* traces the evolution of the highlighted region around a cluster of Bragg spots, because the rotation angle of the sample is changed 19° in 1° steps. In such a cluster, each spot is sharply defined, meaning that the scattering is produced from a single-crystal region of the sample. For conventional single-crystal samples, a Bragg spot of angular dimensions <1° would appear only on one image corresponding to a particular orientation of the crystal. In

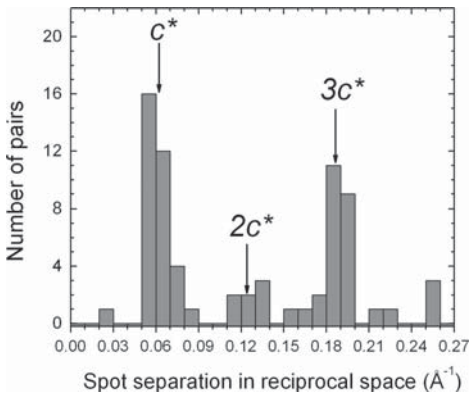

Fig. 2. Histogram of the distribution of distances between the pairs of adjacent Bragg peaks along the *c**-axis in reciprocal space (the bin size is 0.01 Å^{-1}). The positions of *c** at 0.062 Å^{-1}, 2*c**, and 3*c** are marked by arrows. The *c** has been calculated as explained in the text.

the ribbon case, however, the spots appear at multiple adjacent images, and thus form arc segments of ≈6° in reciprocal space. In the inset of Fig. 1, spots of the same color have the same Q vector and thus belong to the same ''Bragg arc.'' The most likely explanation for these arcs is that the strips are not flat but are curved by several degrees even when stretched across the mounting loop. Also note that the scattering volume is small, of the order of 1,000–2,000 μm^3, and hence the Bragg peaks are broad, so that only the strongest peaks are detectable.

To analyze the diffraction patterns that contain such arc-like Bragg reflections, we have developed our own data analysis software. The algorithm that was used for indexing the Bragg peaks and determining the unit cell size is as follows. We manually identified a small area around each spot to be used for analysis. These areas were then analyzed to determine the background intensity and most importantly, the exact position (center of gravity) of each spot. The positions of all selected spots were stored for analysis. This procedure was repeated for all values of the rotation angle, thus reconstructing the 3D reciprocal space of our sample. We reconstructed the ''Bragg arcs'' by following the spots across neighboring angular positions of the sample. The coordinates of the centers of the ''Bragg arcs'' are taken to be the actual Bragg reflections, which would occur if the samples were flat. The total intensities of the entire Bragg arc could not be reliably determined from the data on just the few observed spots. Thus, it was not possible to reconstruct the molecular structure within the unit cell.

Using the location of the Bragg reflections, we reconstructed the corresponding reciprocal space lattice. In this lattice, we observed a family of parallel lines, each of which is formed by closely spaced distinct points. These lines are parallel to one of the coordinate axes of the reciprocal space, the c^*-axis. The displacement vector connecting each pair of observed spots appears identical within integer multiples. The actual distribution of spacings is shown as a histogram in Fig. 2. Here we see a peak at the spacing $c^* = (0.062 \pm 0.003)$ Å^{-1}. We also see a very prominent and well defined peak at $3c^*$. The direction of $\boldsymbol{c^*}$ was found by averaging the displacement vectors connecting adjacent spots along each line. The magnitude of c^* was determined from the distribution of the spacings between adjacent spots in each and every line. After c^* was determined, the vectors $\boldsymbol{a^*}$ and $\boldsymbol{b^*}$ were found by separately finding their components perpendicular and parallel to $\boldsymbol{c^*}$. The spots in reciprocal space were first projected into a plane perpendicular to $\boldsymbol{c^*}$. Next, the components of $\boldsymbol{a^*}$ and $\boldsymbol{b^*}$ perpendicular to $\boldsymbol{c^*}$ were fit to the projected spots by using a least squares fit. As a result, the Miller indices h and k were calculated for all spots. The components of

BIOPHYSICS

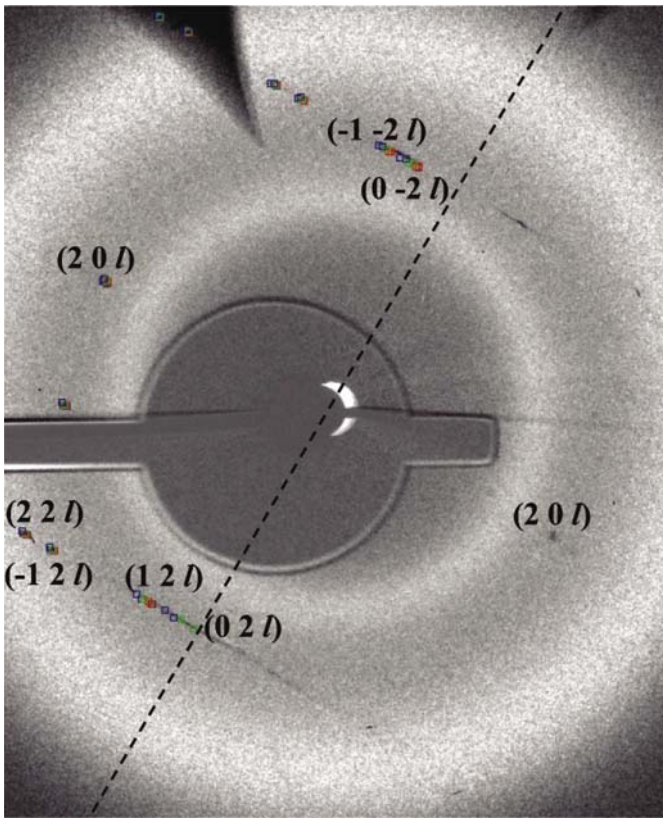

Fig. 3. Diffraction pattern from a helical ribbon formed in model bile. Comparison between diffraction patterns from helices formed in model bile and in CDLC. To the right of the dashed line, we show the pattern of Bragg reflections produced by the single whole helical ribbon formed in model bile. These reflections are spread out, because the curled helix presents a variety of orientations of the crystal to the incoming beam. The experimental data are symmetrical about the dashed line, which is parallel to the axis of the helical ribbon sample. To the left side of the dashed line, we overlaid the observable Bragg reflections with their predicted positions. These predicted positions were calculated by using our analysis of the data found for strips grown in CDLC. Different Miller indices along the c axis are shown by different colors. The broad rings are from the solvent, and the dark area at the center is a shadow of the beam stop. The dark wedge at the upper left corner is an artifact.

a^* and b^* parallel to c^* were then fit to the original (nonprojected) spots, weighted by total spot intensity. The final Miller index, l, associated with the basis vector c^* was calculated at this stage. This completes the indexation of every spot in reciprocal space.

Using the procedure explained above, we found the dimensions of the unit cell. The unit cell parameters at 100 K are: $a = (12.0 \pm 0.2)$ Å, $b = (12.0 \pm 0.2)$ Å, $c = (102 \pm 5)$ Å, $\alpha = (89 \pm 3)^o$, $\beta = (97 \pm 3)^o$, $\gamma = (101.1 \pm 1.7)^o$ (α, β, and γ are the angles between b and c, c and a, and a and b axes, respectively). At room temperature: $a = (12.1 \pm 0.4)$ Å, $b = (12.1 \pm 0.4)$ Å, $c = (102 \pm 5)$ Å, $\alpha = (90 \pm 3)^o$, $\beta = (97 \pm 3)^o$, $\gamma = (102 \pm 2)^o$. For comparison, the unit cell parameters of ChM at room temperature are $a = 12.39$ Å, $b = 12.41$ Å, $c = 34.36$ Å, $\alpha = 90.04^o$, $\beta = 98.1^o$, $\gamma = 100.8^o$ (26). The difference in the lattice constants at different temperatures and between the ribbons and ChM are within experimental errors, except for c. We wish to stress here that the unit cell dimension along the c axis of our strips is triple that of ChM.

By observation of the actual spatial orientation of our strips relative to the diffraction pattern, we find that the c axis is perpendicular to the strip surface, whereas the edge of the strip lies along the b axis.

To compare the findings above for the flattened relatively thick, CDLC strips in air with the actual helical ribbons in aqueous solutions, we studied the diffraction patterns from helical ribbons grown in model bile. These coiled ribbons were inserted into thin glass capillaries (see *Materials and Methods*). Fig. 3 shows an example of a diffraction pattern from a single helical ribbon coiled inside a capillary. The sample was stationary during the exposure to the x-ray beam. Here there is no need to rotate the sample because the x-ray beam cross-section (50×50 μm^2) is much larger than the radius of these helical ribbons, and the scattering from the whole helical ribbon was collected. As a result, the diffraction pattern contains contributions from all crystal orientations rotated around the axis of the helix. We have modified our data analysis software to include the effect of this rotation. The axis of the helix is parallel to the dashed line in Fig. 3. This figure demonstrates agreement between measured diffraction patterns for small helices in model bile solutions and the calculated diffraction pattern for the helix having the crystal structure of CDLC. It is not feasible to accurately deduce the lattice parameters of helices in model bile solutions solely from the observed diffraction patterns. Nevertheless, the comparative x-ray data analysis above strongly supports the view that the crystal structures of the two materials are consistent with one another. This bears out the observation that both materials produce ribbons with identical pitch angles.

Discussion

The unit cell geometry of the helical ribbon crystals has key elements very similar to that of ChM. ChM crystallizes in a quasi-2D structure. The adjacent layers of cholesterol are separated by a layer of water molecules. There is one water molecule per cholesterol adjoining an hydroxyl group. The *ab* plane is parallel to the sheet of the hydrogen-bonded oxygen atoms (26, 27). In helical ribbons, the in-plane dimensions of the unit cell (a, b) and the angles α, β, and γ are very close to those of ChM. Furthermore, in crystalline ChM, the molecules in the unit cell have translational pseudosymmetry in the *ab* plane (28). This pseudosymmetry results in the systematic absence of (h,k,l) reflections, where both h and k are odd. In helical ribbons, we also observed that when both h and k are odd, the reflections are absent. Both these observations demonstrate that the packing arrangement of cholesterol molecules in ChM, and the helical ribbons from both CDLC and model bile must be very similar insofar as the *ab* plane is concerned.

However, notable differences exist between ChM and helical ribbons in both crystal structure and crystal shape. Insofar as the crystal structure is concerned, the difference is in the arrangement of the layers of cholesterol molecules along the c axis. In the ribbons, the out-of-plane unit cell size is three times larger than that of ChM. All other dimensions of the unit cell of the ribbons are the same as those of ChM, within experimental error. From the experimental observation that about one-half of the observed spots are separated by $3c^*$, it is clear that the main structural periodicity is at one-third of the c axis length. This periodicity corresponds to the bilayer thickness of 34 Å and produces the reflections separated by $3c^*$. The existence of spots, which are separated by c^*, as shown in Fig. 2, is evidence of a three-layer superlattice. We observed that the spots separated by c^* do not appear in the (h,$-h$,l) plane. This means that the relative shift of bilayers is along the diagonal of the unit cell in real space, i.e., the [110] crystal direction. Electron diffraction images also show evidence for the formation of a superlattice modulation in the crystal structure of helices formed from model bile (figure 3*D* in ref. 24). The registration of the bilayers can be altered by a different pattern of water molecules between the layers. An illustrative analogy is the crystal structure of the cholesterol derivative stigmasterol, which has been reported recently (29). The overall packing of stigmasterol molecules is

similar to that of cholesterol, but with less than one water molecule per sterol, thus forming a stigmasterol hemihydrate. Another possible cause of the periodic slippage of the layers relative to each other could be the spontaneous deformation of the strip into the helical form. Indeed, because the layers of the inner and outer surfaces of the helix must be of different lengths, slippage of layers should occur, and this could result in a superlattice structure.

In view of the fact that the ribbons are precursors on the pathway to ChM crystals, it is unlikely that surfactant molecules are incorporated between cholesterol layers. We therefore do not believe that surfactant molecules contribute to the triplication of the *c* axis.

Recent studies of cholesterol crystal nucleation upon an air–water interface (29, 30), as well as diffraction electron microscopy studies of cholesterol films in bile (24), cast additional light on the pathway by which helical ribbons may be formed. Both studies show that thin cholesterol crystals have rectangular unit cell, with $a = 10$ and $b = 7.5$ Å. As the thickness increases, the rectangular unit cell transforms into the triclinic unit cell of bulk ChM (30). A striking difference between the rectangular and triclinic structures of ChM exists in the hydrogen-bonding arrangement of the water molecules interleaving the cholesterol layers. In the triclinic ChM, the mesh of the hydrogen bonds is relatively isotropic, whereas in the rectangular cell crystals, the hydrogen bonds generate a stripe-like network, which is oriented along *b* (30). Our work, as well as that of ref. 23, shows that the direction of preferential growth of the ribbons is along *b*. This may be the consequence of the anisotropy of the hydrogen bond network. We suggest that this preferential growth may initially produce elongated strips of rectangular unit cell. As these initial strips grow thicker, the arrangement of cholesterol layers converts to the triclinic lattice of ChM, which we observe. It is conceivable that, during the growth process, the rearrangement of water molecules between layers lags behind the rearrangement of cholesterol molecules and produces a hybrid structure showing the observed superlattice modulation along the *c* direction.

We have demonstrated that the helical ribbons having pitch angle of 11° in CDLC and model bile are constituted of coiled single-crystal strips. These strips have a crystal structure very similar to that of ChM. The essential difference between these two structures is in the tripling of the size of the unit cell along the *c* axis for our helices. The plane of the strip lies in the *ab* plane, whereas the direction of preferred growth, i.e., the long edge of the strip lies along the *b* axis. Because the angle between *a* and *b* axes is 101°, the angle between the perpendicular to the edge of the ribbon and the *a* axis is 11°, which coincides with the observed pitch angle. Thus, it appears that the preferential bending direction in low-pitch helices is along the *a* crystallographic axis.

Materials and Methods

We have measured low-pitch helical ribbons formed in two different solutions. First, we used commercially available CDLC, purchased from GIBCO (Invitrogen, Chicago, IL). CDLC is a water solution that contains nonionic surfactants (Pluronic F-68 and Tween 80), a mixture of fatty acids and cholesterol. The molar ratio (%) of these components is 94.2:1.9:3.9. CDLC produces, with high yield, helical ribbons which remain stable for weeks. The helices in CDLC are rather large and have radii ranging from 5 to 100 μm, contour lengths between 150 and 1,500 μm, and widths between 1 and 20 μm.

As a second solution, we prepared model bile, according to the protocol from ref. 2. Model bile is a water solution that contains common bile salt (sodium taurocholate), lecithin (1,2-dioleoyl-glycero-3-phosphocholine), and cholesterol ($C_{27}H_{46}O$) in molar ratio 97.5:0.8:1.7. Lipid films were prepared as described in ref. 1. The films were diluted in filtered (0.22-μm pore size) Milli-Q (Millipore, Billerica, MA) water at room temperature to a total lipid concentration of 70 mg/ml to obtain a micellar solution nearly saturated with cholesterol. We then added filtered water to bring the solution to a total lipid concentration of 12 mg/ml. This dilution would act to reduce the monomer concentration of surfactant, were it not for the requirement of thermodynamic equilibrium between monomers and micelles. This equilibrium results in transfer of surfactant from micellar to monomer pool, to maintain the critical micellar concentration of the surfactant monomers. The withdrawal of surfactant from the micelles results in supersaturation of the cholesterol solubilized inside the micelles and initiates the formation of helical ribbons, and subsequent emergence of cholesterol crystals. Helical ribbons of both 11° and 54° appear abundantly after ≈5 days after supersaturation, but the ribbons are mostly smaller than those found in CDLC.

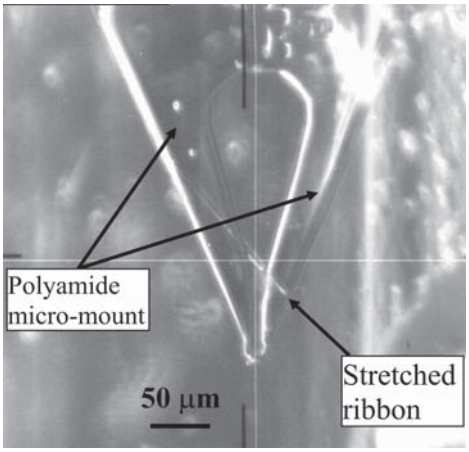

Fig. 4. Photograph of a ribbon on a polyamide micromount (MiTeGen). The 10-μm-wide ribbon is seen as the diagonal strip cutting across the cross-hairs. It is held at the opposite rims of the mount by surface tension. The mount, along with the ribbons, is rotated continuously during x-ray exposure. The rotation axis is approximately vertical on the photograph. The beam center is at the cross-hair. The beam size is 100 × 100 μm.

We conducted diffraction measurements in two configurations: (*i*) helical ribbons stretched flat and mounted on thin nylon loops in air and (*ii*) helical ribbons in their native helical form in solution inside glass capillaries. The advantage of *i* is the absence of background scattering. We used this method to study relatively thick sturdy ribbons like those found in CDLC. However, removal from solution can damage the delicate ribbons such as those found in model bile. To address this issue, we used configuration *ii* to study helical ribbons in their native environment. Insofar as the diffraction measurements are concerned, configuration *i* is clearly superior. Indeed, the best diffraction patterns were obtained from ribbons mounted flat in air. To mount the samples in configuration *i*, a solution with the ribbons was placed on a microscope slide under stereo microscope. The ribbons have a refractive index, which is very similar to that of water. Therefore, we used oblique illumination light source attached to the microscope. The reflections of light from the edges of the ribbons help in forming a 3D image of the ribbons in the solution. The ribbons were removed from the solution by using thin wires or glass capillaries mounted on micromanipulators. The ribbons were stretched across thin nylon loops (Hampton Research, Ariso Viejo, CA) or polyamide micromounts (MiTeGen, Ithaca, NY) of suitable size. Fig. 4 shows an example of a stretched ribbon mounted on a polyamide micromount. In configuration *ii*, we used manual microinjectors (Cell-Tram from Eppendorf, Westbury, NY) to gently manip-

ulate individual ribbons into the capillaries. After trapping a ribbon inside a capillary, the capillary was sealed and immediately placed into the x-ray beam for measurements. In this case, significant background scattering is present. Furthermore, the scattering occurs from the fully curved ribbons having a continuous rotation of the crystalline lattice. This spreads out the Bragg peaks, reducing their intensity and complicating the structural analysis.

X-ray diffraction measurements of biological crystals are routinely done at liquid nitrogen temperatures to reduce radiation damage; we performed both low- (100 K) and room-temperature (300 K) measurements. For the 100 K measurements, the nylon loops were first dipped into oil (Paratone-N from Hampton Research) to form a thin spanning film, and the strips were placed on top of the oil film. The oil enables the strips to remain attached to the loop during flash freezing in liquid nitrogen. The oil was not used for the room temperature measurements.

In both CDLC and model bile, optical observations suggested that the radius of the ribbons grows with their thickness. (According to the elastic model mentioned above, $R \sim t^3$.) Thinner ribbons curl into full helices, whereas thicker ones form rings or arcs, as R becomes too large for a strip of a certain length to form a full helix. We mounted and measured both arc-like strips and full helical ribbons, but the most clear diffraction patterns suitable for detailed analysis were obtained from the thicker arc-like strips. By comparing the patterns from the arcs and fully curved helices, we confirmed that the crystal structure of the helical ribbons is consistent with that of the arc-like ones.

X-ray diffraction experiments were carried out at the Advanced Photon Source, Argonne National Laboratory (Argonne, IL). We used the protein crystallography beamline at Sector 31 (SGX-CAT). A horizontal monochromatic beam of E = 12.66 keV (λ = 0.98 Å) hits the sample, and scattered photons are registered with the CCD detector (MAR 165). To observe Bragg diffraction, the Laue condition must be met, $\mathbf{Q} = \mathbf{k}_f - \mathbf{k}_i = \mathbf{G}$, where $\mathbf{Q}$ is the scattering vector, $\mathbf{G}$ is the reciprocal lattice vector, and $\mathbf{k}_i$ and $\mathbf{k}_f$ are the wave vectors of incoming and scattered photons, respectively. Because $\mathbf{k}_i$ is constant for the incident monochromatic beam, the sample must be rotated to allow $\mathbf{Q}$ to span the reciprocal lattice to observe multiple Bragg peaks. In our setup, the sample rotates around a fixed axis perpendicular to the beam. The rotation speed is constant and the diffraction images are read from the CCD usually every 1° or 2°. The size of the x-ray beam was 50 × 50 μm^2 to 100 × 100 μm^2.

We thank Kevin L. D'Amico, Stephen R. Wasserman, and John W. Koss for support during the measurements at the SGX-CAT beamline at the Advanced Photon Source at Argonne National Laboratory. We thank Fred M. Konikoff, Leslie Leiserowitz, and Yeshayahu Talmon for numerous useful discussions. This work is supported by the U.S. Department of Energy, Division of Materials Sciences and Engineering, Office of Basic Energy Sciences, under Award No. DE-FG02-04ER46149. Use of the Advanced Photon Source was supported by the U.S. Department of Energy, Office of Science, Office of Basic Energy Sciences, under Contract No. DE-AC02-06CH11357. Use of the SGX Collaborative Access Team (SGX-CAT) beamline facilities at Sector 31 of the Advanced Photon Source was provided by SGX Pharmaceuticals, Inc., who constructed and operates the facility.

1. Konikoff FM, Chung DS, Donovan JM, Small DM, Carey MC (1992) *J Clin Invest* 90:1155–1160.
2. Zastavker YV, Asherie N, Lomakin A, Pande J, Donovan JM, Schnur JM, Benedek GB (1999) *Proc Natl Acad Sci USA* 96:7883–7887.
3. Yager P, Schoen PE (1984) *Mol Crys Liq Crys* 106:371–381.
4. Nakashima N, Asakuma S, Kunitake T (1985) *J Am Chem Soc* 107:509–510.
5. Georger JH, Singh A, Price RR, Schnur JM, Yager P, Schoen PE (1987) *J Am Chem Soc* 109:6169–6175.
6. Fuhrhop JH, Schnieder P, Boekema E, Helfrich W (1988) *J Am Chem Soc* 110:2861–2867.
7. Thomas BN, Corcoran RC, Cotant CL, Lindemann CM, Kirsch JE, Persichini PJ (1998) *J Am Chem Soc* 120:12178–12186.
8. Thomas BN, Lindemann CM, Clark NA (1999) *Phys Rev E* 59:3040–3047.
9. Servuss RM (1988) *Chem Phys Lipids* 46:37–41.
10. Schnur JM (1993) *Science* 262:1669–1676.
11. Helfrich W (1973) *Z Naturforsch C* 28:693–703.
12. de Gennes PG (1987) *C R Acad Sci Paris* 304:259–263.
13. Lubensky TC, Prost J (1992) *J Phys II France* 2:371–382.
14. Chen CM (1999) *Phys Rev E* 59:6192–6195.
15. Helfrich W (1986) *J Chem Phys* 85:1085–1087.
16. Helfrich W, Prost J (1988) *Phys Rev A* 38:3065–3068.
17. Ouyang ZC, Liu JX (1990) *Phys Rev Lett* 65:1679–1682.
18. Chung DS, Benedek GB, Konikoff FM, Donovan JM (1993) *Proc Natl Acad Sci USA* 90:11341–11345.
19. Selinger JV, Schnur JM (1993) *Phys Rev Lett* 71:4091–4094.
20. Selinger JV, MacKintosh EC, Schnur JM (1996) *Phys Rev E* 53:3804–3818.
21. Selinger JV, Spector MS, Schnur JM (2001) *J Phys Chem B* 105:7157–7169.
22. Konikoff FM, Cohen DE, Carey MC (1994) *Mol Crys Liq Crys* 248:291–296.
23. Wang D, Carey M (1996) *J Lipid Res* 37:606–630.
24. Weihs D, Schmidt J, Goldiner I, Danino D, Rubin M, Talmon Y, Konikoff FM (2005) *J Lipid Res* 46:942–948.
25. Smith B, Zastavker YV, Benedek GB (2001) *Phys Rev Lett* 87:278101.
26. Craven BM (1976) *Nature* 260:727–729.
27. Craven BM (1986) in *Handbook of Lipid Research*, ed Small DM (Plenum, New York), Vol 4, pp 149–182.
28. Craven BM (1979) *Acta Crystallogr B* 35:1123–1128.
29. Rapaport H, Kuzmenko I, Lafont S, Kjaer K, Howes PB, Als-Nielsen J, Lahav M, Leiserowitz L (2001) *Biophys J* 81:2729–2736.
30. Solomonov I, Weygand MJ, Kjaer K, Rapaport H, Leiserowitz L (2005) *Biophys J* 88:1809–1817.